Materials Today Bio 32 (2025) 101691

Contents lists available at ScienceDirect

Materials Today Bio

journal homepage: www.journals.elsevier.com/materials-today-bio

pH-driven butterfly effect for cascade-amplified tumor therapy based on thalidomide coordinated Fe-HMME nanoplatform

Botao Qu [a,1], Qian Wang [c,1], Yuxin Zhou [d], Xiaogang Ning [e], Qian Wang [f], Ziyi Zhou [b], Peirong Bai [a], Ruiping Zhang [g,*]

[a] Third Hospital of Shanxi Medical University, Shanxi Bethune Hospital, Shanxi Academy of Medical Sciences, Tongji Shanxi Hospital, Taiyuan, 030032, China
[b] School of Basic Medical Sciences, Shanxi Medical University, Taiyuan, 030001, China
[c] School of Forensic Medicine, Shanxi Medical University, Taiyuan, 030001, China
[d] Academy of Medical Sciences, Shanxi Medical University, Taiyuan, 030001, China
[e] School of Chinese Medicine and Food Engineering, Shanxi University of Chinese Medicine, Jinzhong, 030619, China
[f] Department of Medical Imaging, Shanxi Medical University, Taiyuan, 030001, China
[g] The Radiology Department of Shanxi Provincial People's Hospital Affiliated to Shanxi Medical University, Taiyuan, 030001, China

ARTICLE INFO

Keywords:
Photodynamic therapy
Tumor microenvironment
Carrier-free nanoplatform
Butterfly effect
Glutathione depletion

ABSTRACT

A promising approach for treating intractable cancers has been presented by photodynamic therapy (PDT). However, the limited penetration depth of PDT and suboptimal monotherapy efficacy of PDT significantly restrict its clinical applications. In this study, we constructed an acidic tumor microenvironment (TME)-activated carrier-free nanoplatform (HMME-Fe-Thal, abbreviated as HFT) through self-assembly of iron ions, photosensitizer hematoporphyrinmonomethyl ether (HMME) and anti-angiogenesis drug thalidomide (Thal). Near infrared (NIR) triggers PDT behavior before the degradation of the HFT nanoplatform. Subsequently, the HFT nanoplatform degrades, releasing Thal for chemotherapy, iron ions for chemodynamic therapy (CDT), which reinforce the therapeutic benefits of PDT synergistically. Moreover, the iron ions released by HFT degradation turn on the MRI signal, which can suggest the most appropriate time for PDT, divide the treatment into two stages (First-stage: PDT, Second-stage: CDT/chemotherapy), and gradually achieve cascade-amplified tumor therapy. In this sense, HFT modulates TME and leads to a "butterfly effect" of CDT/chemotherapy/glutathione (GSH) depletion for enhanced PDT efficacy. This strategy compensates the deficient shadow penetration and poor treatment efficacy from PDT monotherapy. This work presents the selection and rational design of HFT constructed by endogenous components for tumor regression, and greatly push nanomaterials towards the development of PDT application.

1. Introduction

Photodynamic therapy (PDT), as a promising and noninvasive procedure, has been clinically approved in several countries for treating certain types of cancers due to their controllable and safe characteristics [1–3]. A photosensitizer (PS) absorbs NIR irradiation with a specific wavelength light to activate PS from the ground state (S_0) to the singlet excited state (S_1), followed by undergoing intersystem crossing to triplet excited state (T_1) and generating reactive oxygen species (ROS) [4–6]. It relies on oxidative stress to induce cell apoptosis or ferroptosis through unbalanced redox reactions, lipid peroxidation, mitochondrial and DNA damage [7,8]. Despite the rapid development, PDT has not yet been widely accepted as a first-line tumor treatment due to certain shortcomings including a low penetration depth of light in tissues, and non-negligible dark toxicity [9–11]. More critically, PDT monotherapy cannot fully eradicate tumors because of the complex nature of the tumor microenvironment (TME) [12–14]. It is urgent to investigate the cascade-amplified antitumor behavior to optimize and reinforce PDT strategy for improving tumor treatment efficacy.

The tumor microenvironment (TME) is a complex system characterized by abnormal physiological features, including acidity, hypoxia, nutrient deprivation, metabolite accumulation, and unbalanced redox state [15,16]. To address this complexity, various nanotheranostic systems have been developed for oncotherapy, integrating diagnostic,

* Corresponding author.
E-mail address: zrp_7142@sxmu.edu.cn (R. Zhang).
[1] These authors contributed equally to this work.

https://doi.org/10.1016/j.mtbio.2025.101691
Received 13 January 2025; Received in revised form 5 March 2025; Accepted 20 March 2025
Available online 20 March 2025

therapeutic, and monitoring functionalities into a single nanoplatform [17,18]. TEM activated phototheranostics offer excellent performance and therapeutic effect for oncotherapy, with minimal damage to adjacent normal tissue [19,20]. Activatable phototheranostics with switch on-off mode take full advantage of the specificity of low pH and unbalance redox state in tumorigenesis and progression, allowing for precise manipulation of TME by signal switching from "off" to "on" during cancer diagnosis and treatment [21,22]. The pH-driven disassemble behavior by virtue of substances in TME will lead to a remarkable cancer treatment effect, similar to the butterfly effect [23–25]. Therefore, the relational design of activatable phototheranostic systems aiming at maximizing their anti-tumor ability is crucial.

Nanomaterials have become a rapidly growing research field for designing stimuli-responsive nanotheranostic platforms that can assist in endogenous TME activation or external stimuli [26–28]. Metal-coordinated self-assembly is an elegant strategy that utilizes the coordination force between metal ions and organic ligands to direct the construction of functional materials, and has recently been used to manufacture theranostic nanosystems by combining the superiority of both metal coordination interactions and organic self-assembly [29–31]. For example, Yan et al. designed FMCNPs nanoagents via coordination-driven self-assembly, which performed MRI-guided PDT [32]. Zhang et al. synthesized metal-organic nanodrug complexes (MONCs) by Fe^{3+}-coordinated supramolecular self-assembly of the chemotherapeutic drug doxorubicin (DOX) and photosensitizer DVDMS [33]. However, these delivery systems based on Mn^{2+}, Fe^{3+} or Zn^{2+} element suffer from low biocompatibility and certain toxicity, hindering the clinical translation of metal-based nanodrug. Of note, the iron ion (Fe^{2+}) is essential for key biological pathways including mitochondrial function, oxygen transport and DNA metabolism [34]. Moreover, Fe^{2+} can induce ferroptosis and mediate tumor therapy via chemical dynamics therapy (CDT) due to Fe-catalyzed Fenton reactions facilitated by overexpressed hydrogen peroxide (H_2O_2) in the tumor microenvironment [35,36]. Therefore, the exploration of elaborate Fe^{2+}-coordinated supramolecular nanoassembly with reliable biological security and high-efficient tumor therapeutic effect is still highly challenging.

An elegant nanoplatform with a pH-driven butterfly effect has been fabricated by self-assembling Fe^{2+}, anti-angiogenesis drug Thal, and photosensitizer HMME for carrier-free intracellular delivery. This flexible and environmentally friendly assembly process endows the nanoplatform with several desired attributes: 1) MR signal in quenched state and photosensitization in active state of HFT are shown in normal tissue, but the chemotherapy, MR imaging and CDT functions (from Thal and Fe^{2+}, respectively) can be specifically activated in tumor tissue due to the overexpressed H_2O_2 and lower pH stimulation of TME, reducing side effects to normal tissues; 2) The MRI signal switch from released Fe^{2+} in the nanoplatform not only accomplishes Fenton reaction by reacting with endogenous H_2O_2 to produce highly toxic •OH, but also distinguishes the cascade-amplified therapy process, and concurrently triggers the disassembly, leading to enhanced oxidative stress and therapeutic efficacy; 3) Released Fe^{2+} mediates ferroptosis via lipid peroxidation, further strengthening the tumor treatment outcome; and 4) The CDT/chemotherapy/GSH depletion as an adjuvant for cascade-amplifying PDT therapeutic efficacy by amplification of oxidative stress (Scheme 1). The HFT nanoplatform enables stormy cascade death of tumors through pH-driven-TME stimulation response, similar to butterfly effect, which has the features of safety, low-toxic side effects, and easy metabolism after disassembly, shows great potential for potentiating the clinical applications of PDT in oncology.

2. Experimental section

2.1. Materials

N,N-Dimethylformamide (DMF), Hematoporphyrinmonomethyl Ether (HMME), Thalidomide (Thal) and Iron chloride tetrahydrate ($FeCl_2{\cdot}4H_2O$) were obtained from Sigma-Aldrich. 1,3-

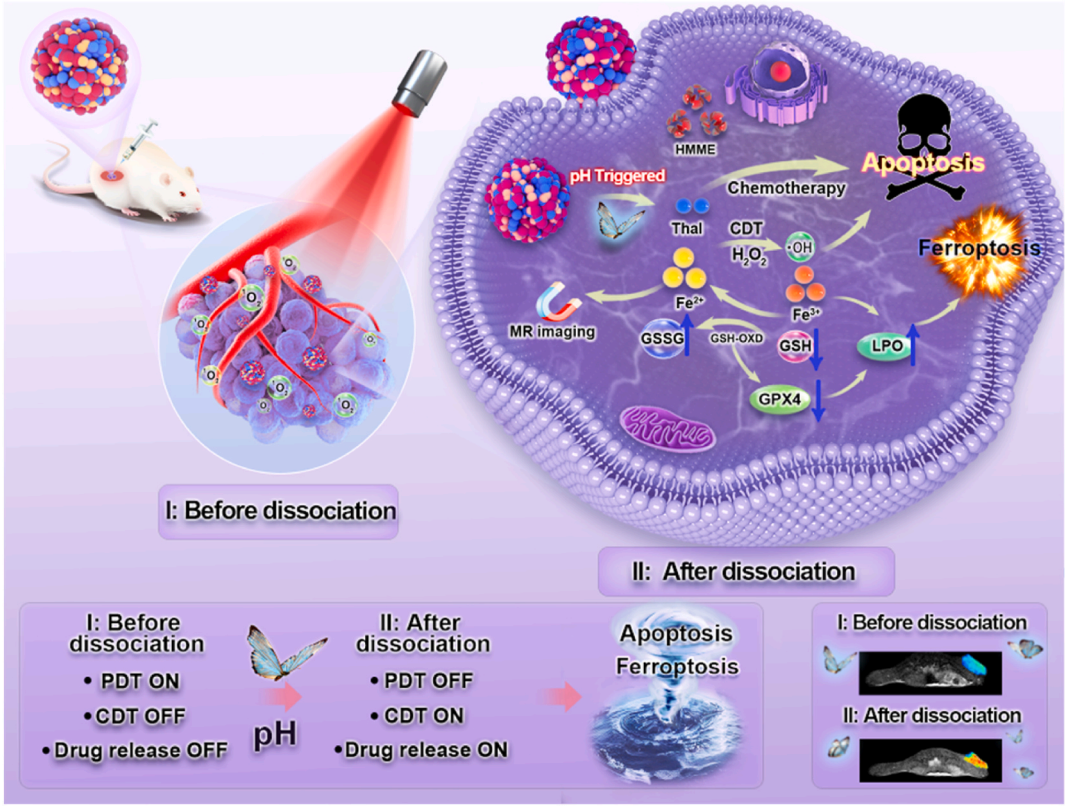

Scheme 1. Schematic illustration of cascade-amplified tumor therapy based on thalidomide coordinated Fe-HMME nanoplatform.

Diphenylisobenzofuran (DPBF), 5,5′-Dithiobis (2-nitrobenzoic acid) (DTNB) and 9,10-Anthracenediyl-bis (methylene) dimalonic Acid (ABDA) were purchased from Alfa Aesar (Tianjin, China). The CCK-8 was provided from Changchun Sanbang Pharmaceutical Technology Co. Ltd. (Changchun, China). 2′,7′-dichloroflfluorescein diacetate (DCFH-DA), and Rhodamine 123 (RH123) were obtained from Nanjing Jiancheng Bioengineering Institute (Nanjing, China). Glutathione peroxidase 4 (GPX4), and β-actin mouse monoclonal antibody were purchased from Abcam. All chemicals were of analytical grade and used without further purification.

2.2. Synthesis of HFT NPs

In brief, 1 mg Thal, 0.5 mg HMME, and 500 μL DMF were mixed and vortexed for 1 min. Then 1 mL $FeCl_2{\cdot}4H_2O$ (10 mg/mL) aqueous solution was added dropwise with violent stirring for 1 min. After ultrafiltration centrifugation (2500 rpm, 15 min) and washing with deionized water for several times, the HMME-Fe-Thal nanoparticles (HFT NPs) were

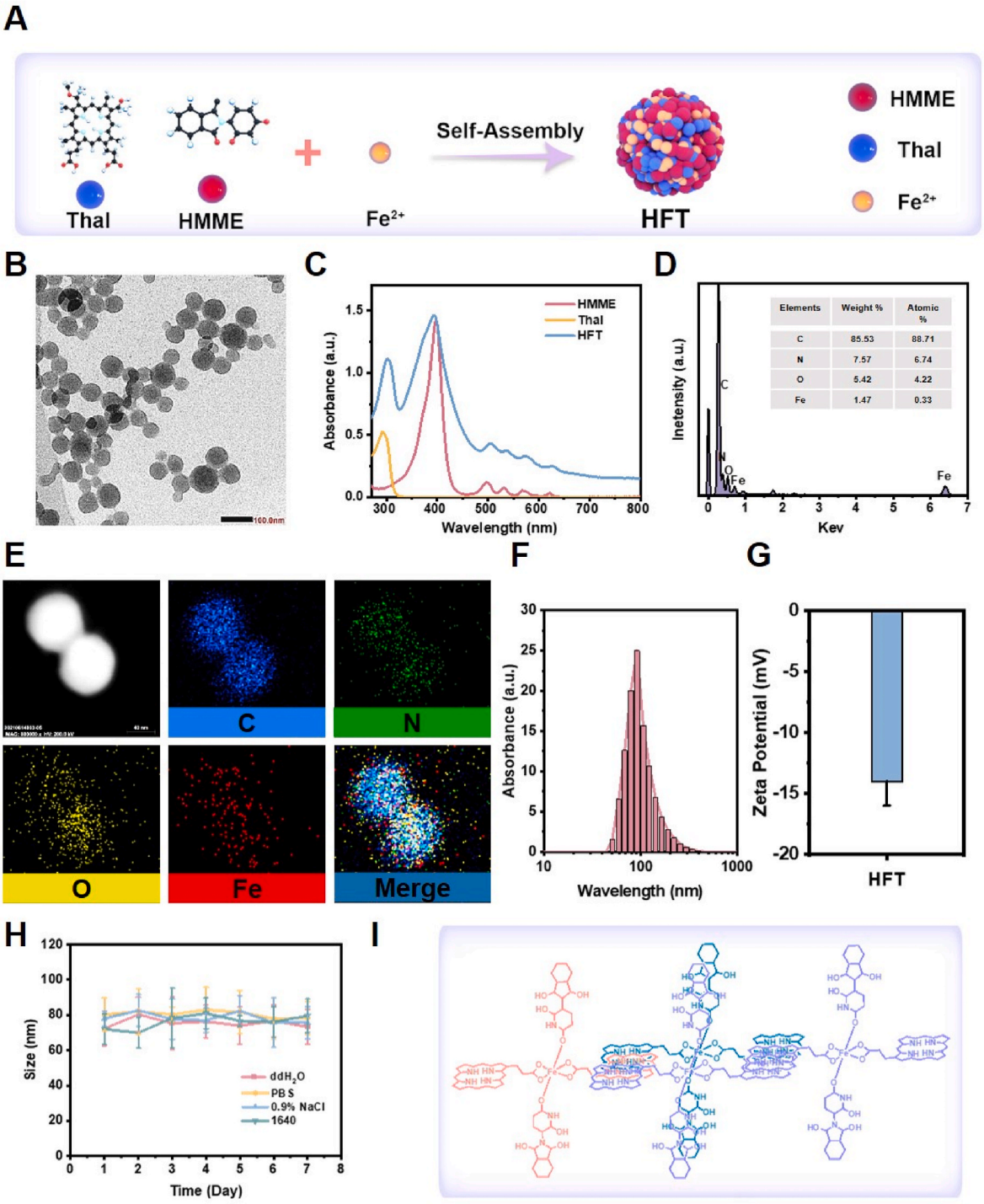

Fig. 1. Characterization of HFT. (A) Schematic illustration of synthetic procedure of HFT. (B) TEM image of HFT. (C) UV–Vis spectra of HMME, Thal and HFT. (D) EDS spectrum of HFT. (E) HAADF-STEM image and EDS elemental mapping of HFT. (F) DLS analysis of HFT. (G) Zeta potential of HFT. (H) Stability of HFT in 8 days. (I) The packing model of HFT from MD simulation.

obtained and stored at 4 °C for further use.

The detailed experimental processes are available in the Supplementary Information.

3. Results and discussion

3.1. Preparation and characterization of NPs

The chemotherapy drug thalidomide (Thal) was chosen for its ability to inhibit angiogenesis by reducing the secretion of vascular endothelial growth factor (VEGF) and fibroblast growth factor (FGF) [37]. The HMME-Fe-Thal nanoplatform (HFT) was created by dropping a thalidomide solution into a mixed solution of HMME and ferrous chloride (Fig. 1A). HFT NPs has a homogeneous monodisperse spherical shape with a smooth surface and an average size of 60 nm, which was verified by transmission electron microscopy (TEM) images (Fig. 1B). Dynamic light scattering measurement was applied to identify the hydrodynamic size of NPs (Fig. 1F). The average hydrodynamic sizes of HFT was gauged to be 100 nm, which were slightly larger than the TEM analysis. The zeta potential of HFT was −13 mv, proving its stability (Fig. 1G). Moreover, the size change of HFT in different buffer solution in 8 days was also studied. Which also revealed that HFT possessed excellent stability. The loading efficiency of Thal was determined to be approximately 68 %. The results of High-angle annular dark-field scanning transmission electron microscopy (HAADF-STEM) were shown that Fe, N, C, and O were homogeneously distributed in HFT (Fig. 1E). Energy-dispersive X-ray spectroscopy (EDS) further confirmed the uniform distribution of these elements (Fig. 1D). The UV/Vis absorption spectrum indicated that HFT exhibited the two characteristic peaks from HMME at 397 nm and Thal at 302 nm (Fig. 1C), suggesting the formation of nanoassemblies. A molecular dynamics (MD) simulation using a density functional theory (DFT) method was conducted to confirm the self-assembly mechanism. The results showed that the coordination environment of Fe^{2+} ion was coordinated with four oxygen atoms from two HMME molecule and two oxygen atoms from two Thal ligands, resulting in a square bipyramid coordination geometry (Fig. S1). The adjacent secondary building units (SBUs) were stacked into a 3D supramolecular structure through π–π stacking interaction and hydrogen bonding (Fig. 1I).

3.2. Characterization of tumor microenvironment response of NPs in vitro

The stimuli-responsive properties of the nanoplatform were investigated based on the synergy function from coordination and hydrogen bonding and π–π stacking interaction. The coordination bonds were found to be responsive to external acidic conditions due to the rivalrous

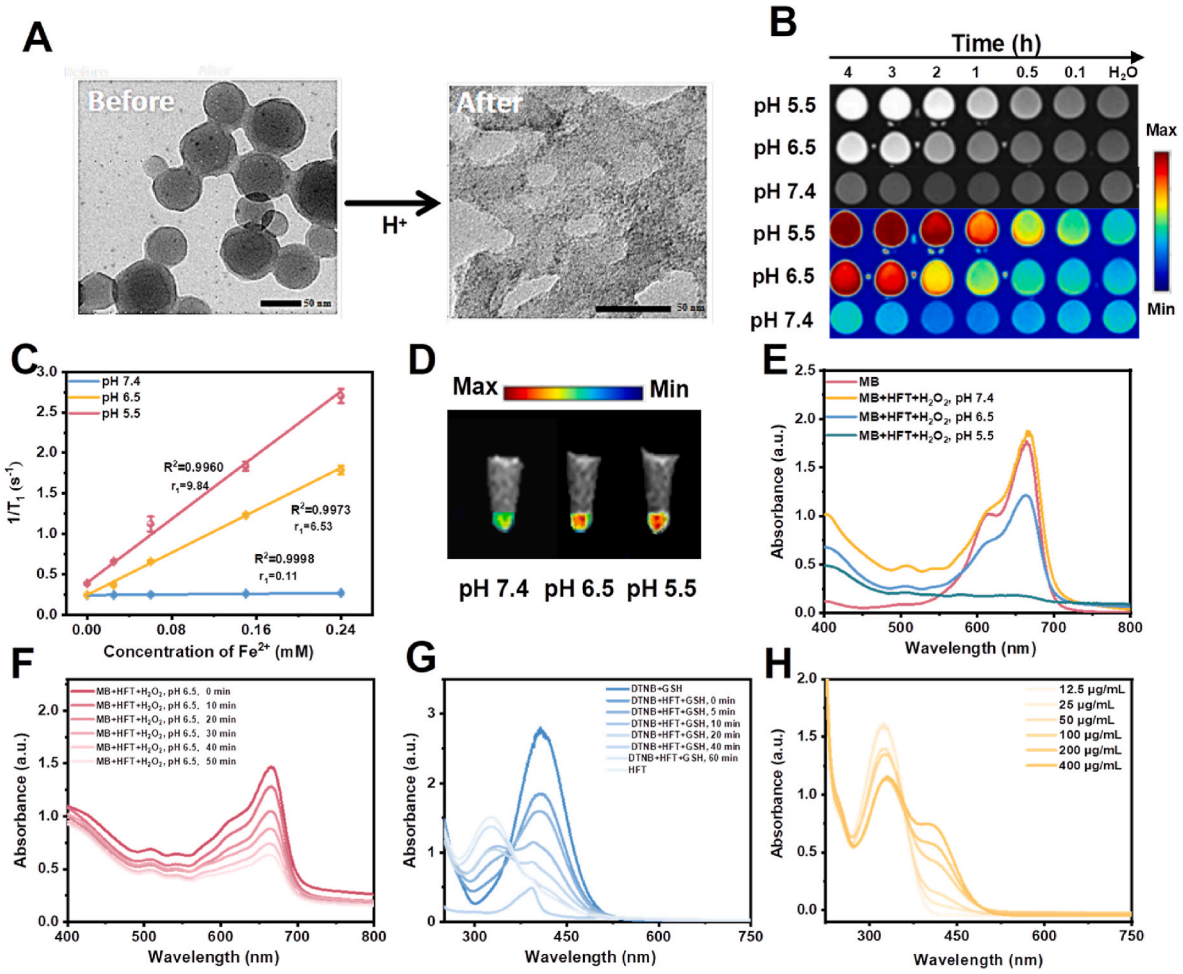

Fig. 2. MRI performance, ROS generation and GSH depletion of HFT before and after degradation. (A) The morphology changes of HFT before and after pH-mediated disassembly. (B) Time-dependent MR images of HFT with different pH values. (C) T_1 relaxivity measurements of HFT in PBS with different pH values. (D) In vitro T_1-weighted MR images of 4T1 cell after incubated with HFT under different pH values. (E) UV–vis spectra and color changes of MB incubated with H_2O_2 and HFT at pH 7.4, 6.5 or 5.5. (F) Time-dependent MB oxidation by •OH from Fenton reaction by the disassembly of HFT. (G) Time-dependent GSH depletion by HFT. (H) UV–vis spectra of the mixtures of different concentrations of HFT, DTNB and GSH. (For interpretation of the references to color in this figure legend, the reader is referred to the Web version of this article.)

bonding between guest molecules with metal ions and protons [38]. The HFT showed excellent pH-dependent degradable behavior in mimic TME, with a drug release rate of 49 % at pH 6.5 and 68 % at pH 5.5 in just 12 min (Fig. S2). The spheric nanoparticle gradually degraded, deforming to a like-jelly structure from the perspective of morphology by TEM (Fig. 2A). The MR image of HFT was recovered in acidic environment when disassembled into fragments (Fig. 2B and S3), accompanying with enhanced MR signal intensity over time, which resulted from the continuous release of Fe^{2+} from nanoassembles. The MR signal was activated from 'off' mode to 'on' mode in acidic conditions, with the r_1 value of HFT significantly increasing from 0.11 mM^{-1} s^{-1} at pH 7.4 to 6.53 and 9.84 mM^{-1} s^{-1} at pH 6.5 and 5.5 (Fig. 2C). In vitro MRI at the cellular level also demonstrated that with the acidity increasing the MRI dramatically enhance, implying that the pH-induced MRI switch function (Fig. 2D). This phenomenon also explains the reason why CDT function was shut off in the nanoplatform under neutral condition, but recovered in TME.

Next, we investigated the generation of •OH using MB as a probe under different conditions. The time-dependent absorption changes of MB at 660 nm in HFT suspension containing H_2O_2 at various pH levels were shown in Fig. 2E. This experiment clearly demonstrated that pH-driven Fe^{2+} release could induce the Fenton reaction by reacting with

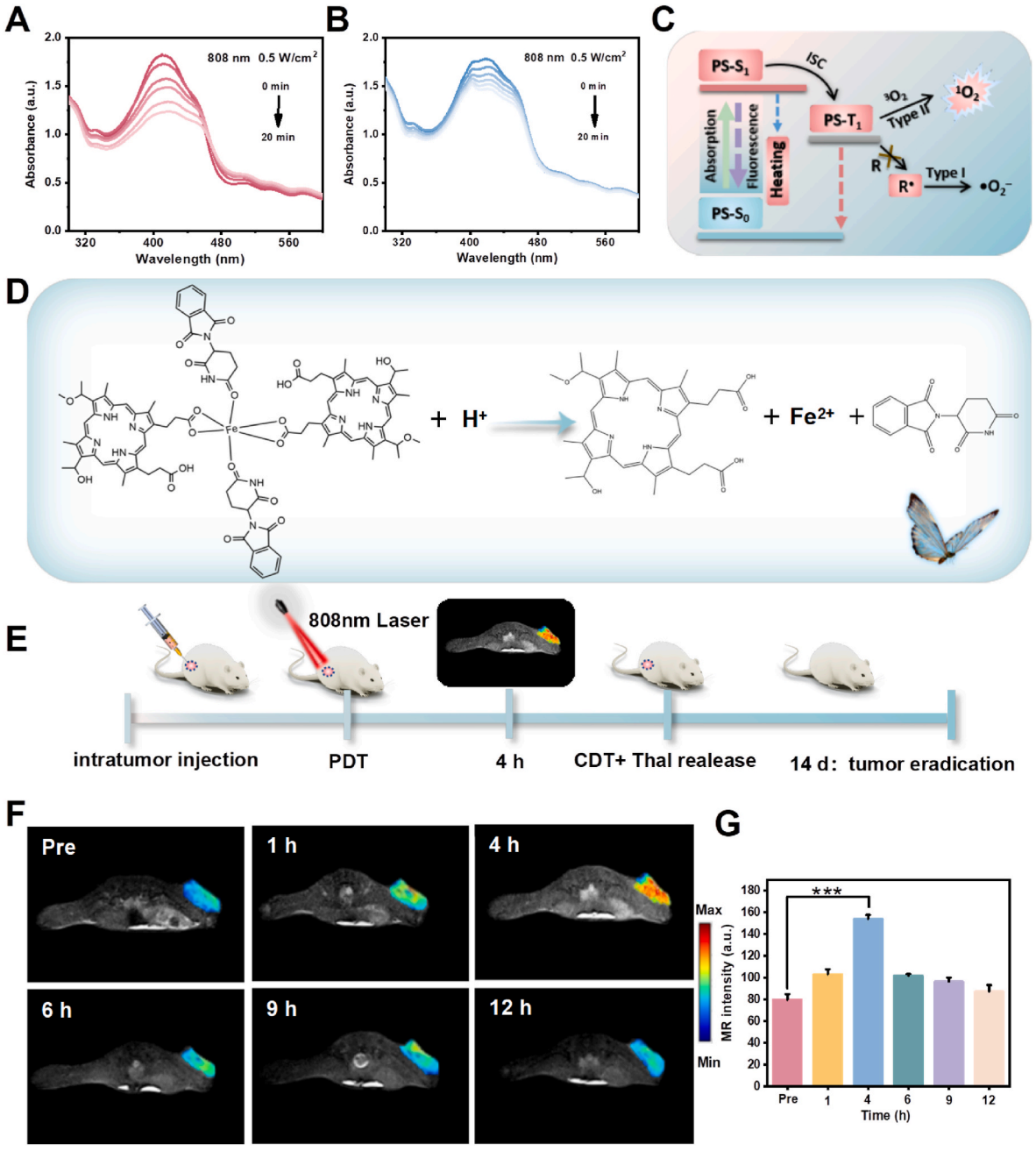

Fig. 3. The mechanism of pH-driven butterfly effect and MRI-monitored subsection of first-stage PDT and second-stage CDT. (A) DPBF oxidation curves of HFT at different time points at pH 7.4 under 808 nm light exposure (0.5 W/cm^2). (B) Time-dependent oxidation of DPBF after pH-activated HFT under 808 nm laser irradiation (0.5 W/cm^2). (C) Schematic illustration of the possible mechanism of $^1O_2$ generation. (D) The mechanism driving the butterfly effect of HFT. (E) Schematic illustration of MRI-monitored subsection of first-stage PDT and second-stage CDT process. (F) Representative in vivo T_1-weighted MR images of 4T1 tumor-bearing mice at various time points before and after i.t. injection of HFT. (G) Relative MR signal intensity in tumor in Fig. 3F. Mean ± SD (n = 3). *p < 0.05, **p < 0.01, ***p < 0.001. Student's t-test.

H_2O_2. In the HFT solution plus H_2O_2, the characteristic absorption peak of MB was observed. However, after adjusting the solution to pH 6.5 and pH 5.5, the MB absorption spectrum quickly vanished. The characteristic peak of MB gradually decreased with increasing reaction time, indicating the HFT s' excellent ability to produce •OH (Fig. 2F). We also explored the GSH depletion ability of HFT using the DTNB probe, which showed that the HFT could effectively react with GSH in a time and concentration-dependent manner (Fig. 2G and H).

3.3. Photodynamic therapy of NPs monitored by magnetic resonance imaging

We subsequently investigated the "on"-"off" behavior of PDT before and after the activation of pH value. 1,3-Diphenylisobenzofuran (DPBF) was employed as a singlet oxygen ($^1O_2$) chemical probe to detect $^1O_2$ production triggered by 808 nm laser irradiation. Under neutral condition, the characteristic absorption of DPBF at 410 nm decreased gradually as the duration of laser irradiation was prolonged for 20 min. After activation under acidic condition, the production of $^1O_2$ was clearly suppressed (Fig. 3A and B). The similar result was confirmed by ABDA experiment (Fig. S4). This phenomenon can be accounted for by a certain fact that H^+ ions destroy the J-aggregation structure of HMME in HFT followed by the formation of HMME molecular aggregates, leading to the switch off of PDT [39,40]. The possible mechanism of $^1O_2$ is shown in Fig. 3C. J-aggregation provided smaller energy gap between the lowest singlet and triplet excited states for an efficient intersystem crossing (ISC), facilitating photoinduced $^1O_2$ generation. The process of PDT switches on-off realized efficient off-on pH-switching of MRI, CDT, and chemotherapy function. Importantly, the MRI could better evaluate the subsection of PDT and CDT process. The mechanism driving the butterfly effect of HFT was elaborated based on the chemical reaction. As shown in Fig. 3D, the HFT can rapidly decompose to release HMME and Thal molecule, simultaneously generating a large quantity of Fe^{2+} ions through pH-driven butterfly effect. The releasing Fe^{2+} ions not only perform MRI function but also endow CDT function by Fenton reaction reacted with overexpressed H_2O_2 in tumor tissue, and the releasing Thal implements chemotherapy against tumor cell. This intriguing phenomenon exquisitely achieves MRI-monitored the subsection of PDT and CDT process, contributing to choose therapeutic method suitably for maximizing anti-tumor efficacy.

3.4. Characterization of NPs at the cellular level

To confirm the results of the previous experiments, an in vivo experiment was conducted using a 4T1 tumor xenograft model. The HFT was injected intratumorally in tumor-bearing mice. The MR signal intensity in the tumor site reached its maximum after 4 h with a 2-fold elevation, indicating the TME-activated degradation of HFT (Fig. 3E and F). This time node provides a precise evaluation of the PDT and CDT process, with the most appropriate time for PDT being before 4 h. The PDT function was shut off with extended post-injection times, while the CDT, MRI, and chemotherapy functions were recovered at 4 h after injection, indicating their predominant role at each stage in the process of tumor treatment (Fig. 3G). Consequently, MRI plays a pivotal role in monitoring the treatment modality across different stages. Two-stage therapy, including the first-stage PDT and second-stage CDT/chemotherapy, can be effectively monitored by MRI for maximizing treatment effect.

The cell uptake of the nanoplatform was evaluated prior to tumor therapy, given the unique features of HFT in the TME. 4T1 cells were incubated with HFT for varying time periods, and fluorescent images and flow cytometry analysis revealed that the red fluorescence signal intensity from HFT gradually increased as the incubation time increased (Fig. 4A and B and S5). The internalized HFT was mainly located in the cytoplasm, indicating successful cell uptake of the nanoplatform. Additionally, the mitochondrial targeting ability of HFT was tested using inverted fluorescent microscope. The mitochondria were labeled with a green dye, Mito-Tracker Green, and the red fluorescence signals of HFT were found to be colocalized well with the green fluorescence signals of Mito-Tracker Green, indicating that HFT could efficiently target mitochondria (Fig. 4E).

To investigate the cytotoxicity mechanism of different treatment stages, we used a fluorogenic marker, 2,7-dichlorofluorescein diacetate (DCFH-DA), to detect the production of ROS. According to Fig. 4F and C, there was almost no fluorescence signal in blank cells, and weak green fluorescence signals appeared in HFT-treated cells and HFT-treated cells with H_2O_2, respectively. In contrast, HFT + L group ($^1O_2$ group) and HFT + H_2O_2 + pH 5.5 group (•OH group) showed obvious green fluorescence signal, indicating that the first-stage PDT and second-stage CDT play a critical role in tumor therapy by generating ROS. The green fluorescence of rhodamine 123 notably reduced when the cells were treated in the HFT + pH 5.5 group (Chemotherapy) and HFT + H_2O_2 + pH 5.5 group (CDT/Chemotherapy), suggesting a decrease in ψ_m (Fig. 4G and D). Trypan blue staining further confirmed the efficacy of the two-stage therapy in killing tumor cells (Fig. 4H). The loss of mitochondrial membrane potential also serves as an early indicator of apoptosis via the mitochondrial pathway [41], as analyzed by annexin V-FITC/PI apoptosis experiment (Fig. 4I).

3.5. Characterization of NPs promoting iron death

To evaluate the induction of ferroptosis, we examined the expression of GPX4 using western blotting. The results showed a significant down-regulation of GPX4 in the pH 5.5 + H_2O_2 group, while the pH 6.5 + H_2O_2 group showed a slight downward trend (Fig. 5A–C). Additionally, the GSH content, GSSG content, and GSSG/GSH ratio further confirmed that pH-driven ferroptosis was due to GSH reduction, as confirmed by Elisa analysis (Fig. 5D–F). Malondialdehyde (MDA) was used to monitor lipid peroxide (Fig. 5G). Notably, the MDA content was greatly elevated in the pH 5.5 + H_2O_2 group, indicating the most severe ferroptosis status in this group. The increased concentration of free Fe^{2+} in cells can increase the sensitivity of cells to iron sag disease. Therefore, we examined the intracellular distribution of Fe^{2+} using FeRhonox-1 probes that specifically recognize Fe^{2+}. As shown in Fig. 5H and I, we found that the fluorescence of Fe^{2+} gradually brightened with the extension of the time of cells treated by HFT, indicating that HFT could gradually release Fe^{2+} in cells to enhance iron death. Meanwhile, Bio-TEM was used to observe the cellular ultrastructure of mitochondria under different treatments. As shown in Fig. 4J the HFT + pH 5.5, H_2O_2 group demonstrated a noticeable change in mitochondrial structure, which showed an overtly shrunken shape and thickened and reduced mitochondrial cristae. The aforementioned evidence indicates that HFT can induce ferroptosis in 4T1 cells, ultimately resulting in cell death.

These findings suggest that the pH-driven butterfly effect can achieve a synergistic apoptosis/ferroptosis effect, eventually leading to permanent tumor cell death [42]. A possible mechanism of tumor suppression for HFT is proposed in Fig. 5k. After intratumoral (i.t.) injection, the HFT can generate cytotoxic $^1O_2$ under laser irradiation in the first-stage PDT before degradation. The introduction of HMME endows HFT with ROS generation ability under light irradiation. After 4h incubation, the HFT in the second-stage CDT/chemotherapy, gradually disassemble and the released Fe^{2+} catalyzes endogenous H_2O_2 to generate toxic •OH via a Fenton reaction. The obtained Fe^{3+} by cascade reaction further consumes GSH, leading to lipid peroxides followed by ferroptosis. Meanwhile, the released drug Thal exerts its chemotherapeutic function by anti-angiogenesis effect. Consequently, the abundant amounts of ROS ($^1O_2$ and •OH), the anti-angiogenic effects, and GSH depletion cooperatively increase the level of oxidative stress, ultimately resulting in cell apoptosis.

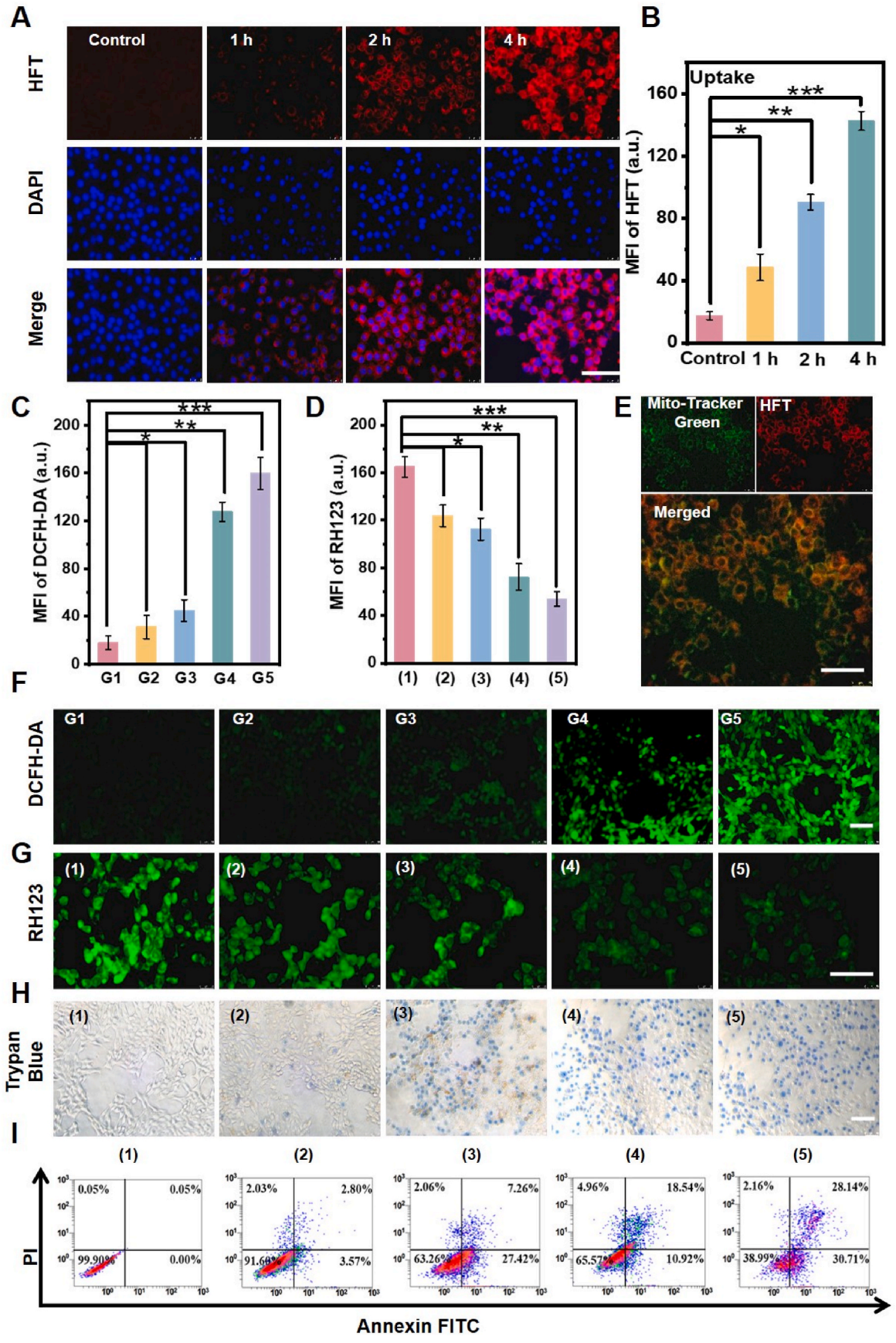

(caption on next page)

Fig. 4. Evaluation of the targeting ability and cell cytotoxicity for HFT NPs. (A,B) Fluorescence images of 4T1 cancer cells incubated with HFT for different time. (C, F) Fluorescence images of 4T1 cells stained with DCFH-DA after different treatments as indicated. (For interpretation of the groups in this figure legend: G1: Control; G2: only HFT; G3: HFT + H_2O_2 G4: HFT + L (808 nm, 0.5 w/cm^2); G5: HFT + H_2O_2 + pH 5.5.) (D,G) Fluorescence images of $\Delta\psi_m$ collapse determined by rhodamine 123. (E) Fluorescence images of immunofluorescent staining by Mito-Tracker Green indicating the intracellular location of HFT. (H) Trypan blue stained images of 4T1 cells incubated with HFT at different treatments. (I) Annexin V-FITC/PI staining for cell apoptosis detected by FCM. (For interpretation of the groups in Figure D and G–I: (1): Control; (2): only HFT; (3): HFT + L (808 nm, 0.5 w/cm^2); (4): HFT + pH 5.5; (5): HFT + H_2O_2 + pH 5.5.). (Scale bar: 100 μm). Mean ± SD (n = 3). *p < 0.05, **p < 0.01, ***p < 0.001. Student's t-test. (For interpretation of the references to color in this figure legend, the reader is referred to the Web version of this article.)

3.6. Tumor inhibition effect of NPs

The therapeutic efficacy of HFT at the cellular level was assessed under different conditions before evaluating its antitumor activity in vivo. The cell viability in the HFT group, HFT + pH 5.5 group, and HFT +808 nm laser group were 82.73 %, 44.09 %, and 27.92 % (Fig. S6), respectively, at a concentration of 200 μg mL^{-1}. After being treated with HFT + H_2O_2 + pH 5.5 group, the cell viability decreased to 22.34 %, demonstrating the potential of HFT as an effective therapeutic agent for killing cancer cells. Based on the above antineoplastic performance, tumor-bearing mice were randomly divided into four groups (n = 4 per group): (1) PBS group (as control); (2) HFT + V_c (vitamin C) group (chemotherapy); (3) HFT group (CDT/chemotherapy); and (4) HFT + L group (PDT/CDT/chemotherapy). Throughout the 14-day treatment period, the tumor volume and body weight of mice in the designated groups were documented continuously. The tumors in the PBS group grew fast, while the tumors in the HFT + V_c group were slightly inhibited, mainly due to the chemotherapy function of Thal (Fig. 6A). In comparison, the HFT group showed a significant tumor inhibition effect, mainly resulting from the synergistic antitumor effect of CDT and chemotherapy. After introducing NIR Laser, HFT with 808 nm laser irradiation provoked the highest tumor regression, which clearly displayed that the two-stage treatment strategy performed the most prominent inhibition of cell proliferation, further verifying the remarkably enhanced efficacy of this triple synergistic treatment (PDT/CDT/chemotherapy) (Fig. 6C and S7). The body weight among all groups depicted inappreciable change (Fig. 6B), confirming the biosafety of HFT.

After treatment, the tumors were collected and subjected to immunohistochemistry characterization (Fig. 6D). The H&E staining of the tumor tissues confirmed that severe cell death was observed in HFT + L group (PDT/CDT/chemotherapy), manifested as nuclear pyknosis and enlarged intercellular space. In contrast, the tumor cells in HFT + V_c group (chemotherapy) and HFT group (CDT/chemotherapy) were slightly damaged compared with the control group. Ki67, TUNEL and GPX4 staining results further verified the significant suppression of cell proliferation, severe cell apoptosis endowed and ferroptosis the two-stage treatment characteristic, which is in accordance with the H&E analysis result (Fig. 6E and F). Meanwhile, the pathological analysis of main organs by H&E assay presented no obvious injury or inflammation (Fig. S8). These results revealed that HFT feature a prominent therapeutic effect and biosafety, which can be ascribed to the endogenous component of degradation and rational design philosophy. The biochemical markers, including the liver and kidney functional indexes, all remained within the normal ranges, further confirming the reliable biosecurity of HFT (Fig. S9). To clarify the cascade amplification effect of HFT nanoplatform, we investigated the therapeutic effect of PDT (HMME + L) and CDT ($FeCl_2$) monotherapy. After 14 days of treatment, the tumor growth was not inhibited in monotherapy. Histological assessments of tumor tissue after treatment via H&E and TUNEL staining revealed minimal apoptosis in monotherapy (Fig. S10). These experiments imply that neither PDT alone nor CDT alone achieved the desired therapeutic outcomes.

To demonstrate the anti-angiogenesis effect of HFT in antitumor therapy, we investigated the vascular density of the tumor site in vivo using photoacoustic imaging. Blood oxygen saturation (sO_2) can be determined based on their strong NIR-I PA signals. We visualized the sO_2 content in tumor tissues at different times before and after treatment. The intratumoral blood flow displayed moderate oxygen levels before HFT injection. However, the tumor site showed a weak signal of sO_2 6h after injection of HFT, implying that HFT exerted a significant anti-angiogenesis effect in tumor tissue by decreasing vascular density. As the treatment time extended, the sO_2 signal was further reduced (Fig. 6H and I). Subsequently, we performed immunohistochemical analyses of VEGF and CD31 to observe vascular hyperplasia. As exhibited in Fig. 6J and S11, the expression of VEGF in tumor tissue was remarkably lower in HFT-treated mice than in the parallel control group. Meanwhile, the microvessel density marker CD31 was dramatically downregulated. It was obvious that the broader brown color increased with the increasing HFT concentration. These results indicate that HFT can strongly inhibit angiogenesis in tumor tissue.

3.7. Mechanism of action of NPs via RNA-seq analysis

To further investigate the antitumor effects of HFT, 4T1 tumor tissue treated with HFT + L or Control (PBS) group were collected for transcriptome analysis. We used DESeq2 to conduct a differential gene expression analysis [43–45]. As depicted in the volcano plot (absolute fold change≥1 and p-values<0.05), a comprehensive analysis was conducted on a total of 25423 genes, resulting in the identification of 1227 differentially expressed genes, which included 618 up-regulated and 609 down-regulated genes (Fig. 7A), implying that HFT + NIR treatment cause obvious change in tumor microenvironment. Differentially expressed genes were subsequently utilized for clustering analysis to generate a heat map (Fig. 7B), which corroborated the significant genetic differences between the two groups. The Venn diagram in Fig. 7C exhibits that, compared with the PBS group, there were 12691 identical and 326 unique differentially expressed genes in HFT + L group compared with PBS group. The significant differences of gene expression highlighted the pronounced discrepancies in the transcriptomic landscape between the HFT + L and PBS groups. To further probe into the biological functions of these genes, we conducted Gene Ontology (GO) and Kyoto Encyclopedia of Genes and Genomes (KEGG) enrichment analyses. The bar chart of GO analysis in Fig. 7D shows that the biological processes of 4T1 tumor tissue treated with HFT + L are primarily focused on reactive oxygen species metabolic process, regulation of angiogenesis, oxidative stress, xenobiotic stimulus, metal ions and fatty acid metabolism [46]. The KEGG enrichment results indicated that these differentially expressed genes induce ferroptosis and apoptosis in HFT + L groups mainly by activating the chemical carcinogenesis-reactive oxygen species, IL-17 signaling pathway PI3K-Akt signaling pathway, TNF signaling pathway, and other related signaling pathways (Fig. 7E) [47,48]. Furthermore, we also observed the upregulation of genes associated with the IL-24, glutathione-s-transferase, IL-1β, as well as downregulation of genes related to the MMP9 and Fgf2 following HFT + L treatment, which corroborated the inhibitory effect on 4T1 (Fig. S12). To gain a deeper understanding of the therapeutic mechanism, gene set enrichment analysis (GSEA) was conducted (Fig. S13). The HFT + L treatment enhanced the expression of genes associated with oxidative stress response, chemical carcinogenesis via reactive oxygen species, the IL-17 signaling pathway, ferroptosis, and the TNF signaling pathway. Transcriptomic analysis lays the groundwork for a comprehensive exploration of the anti-tumor mechanisms of HFT. These findings demonstrate that the thalidomide coordinated

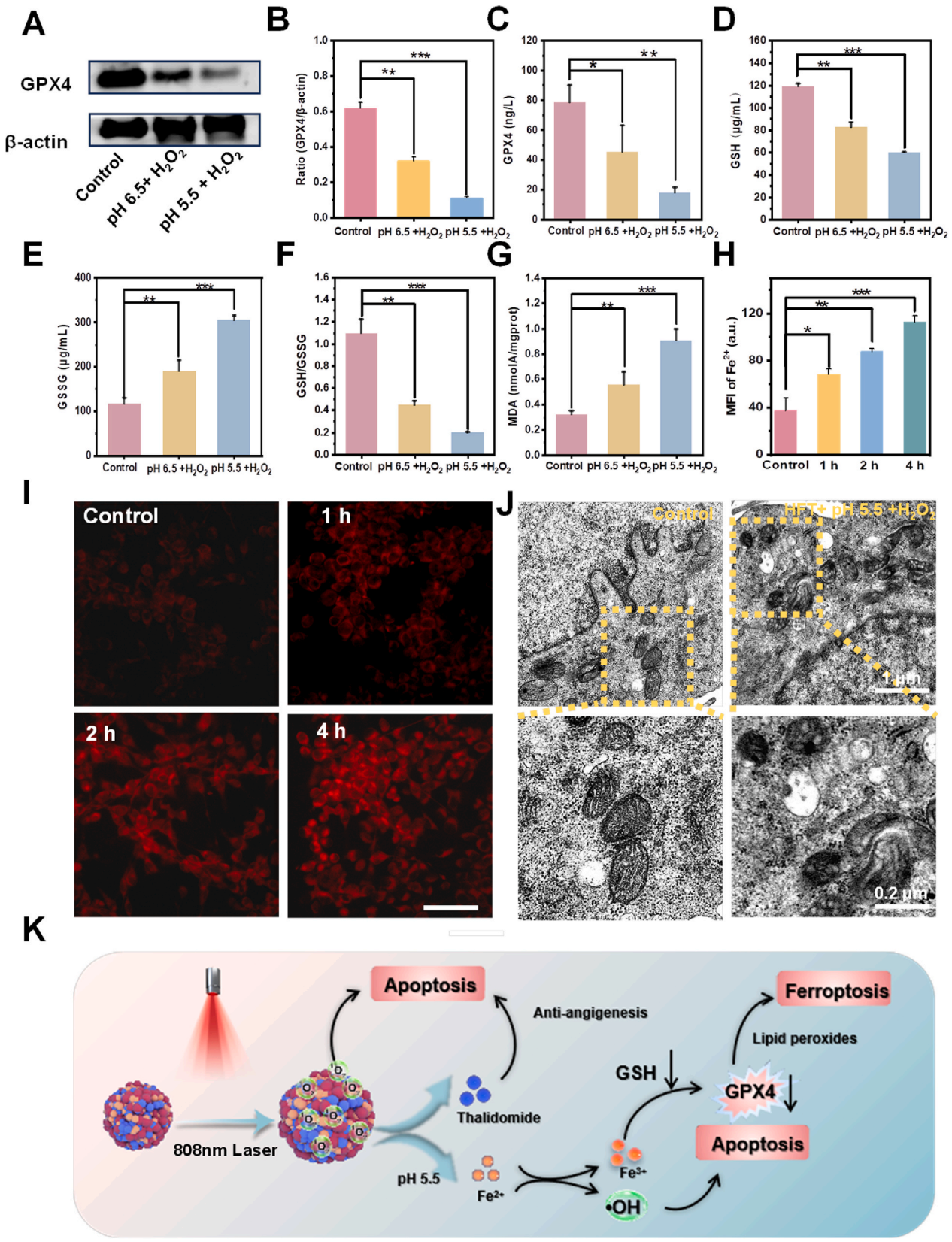

Fig. 5. The evaluation of ferroptosis/apoptosis properties and the anti-tumor mechanism by reinforcing PDT therapeutic efficacy. (A,B) Western blot analysis of GPX4 expression and semi-quantitative ratio (C) GPX4 content (D), GSH content (E), GSSG content (F), GSH/GSSG level (G), and MDA content in 4T1 cells treated with HFT in different conditions. (H, I) The intracellular Fe^{2+} distribution after HFT treatment. (Scale bar: 100 μm). (J) TEM images of 4T1 cells after different treatments. (K) The proposed schematic diagram of HFT-induced ferroptosis/apoptosis by first-stage PDT and second-stage CDT/chemotherapy process. Mean ± SD (n = 3). *p < 0.05, **p < 0.01, ***p < 0.001. Student's t-test.

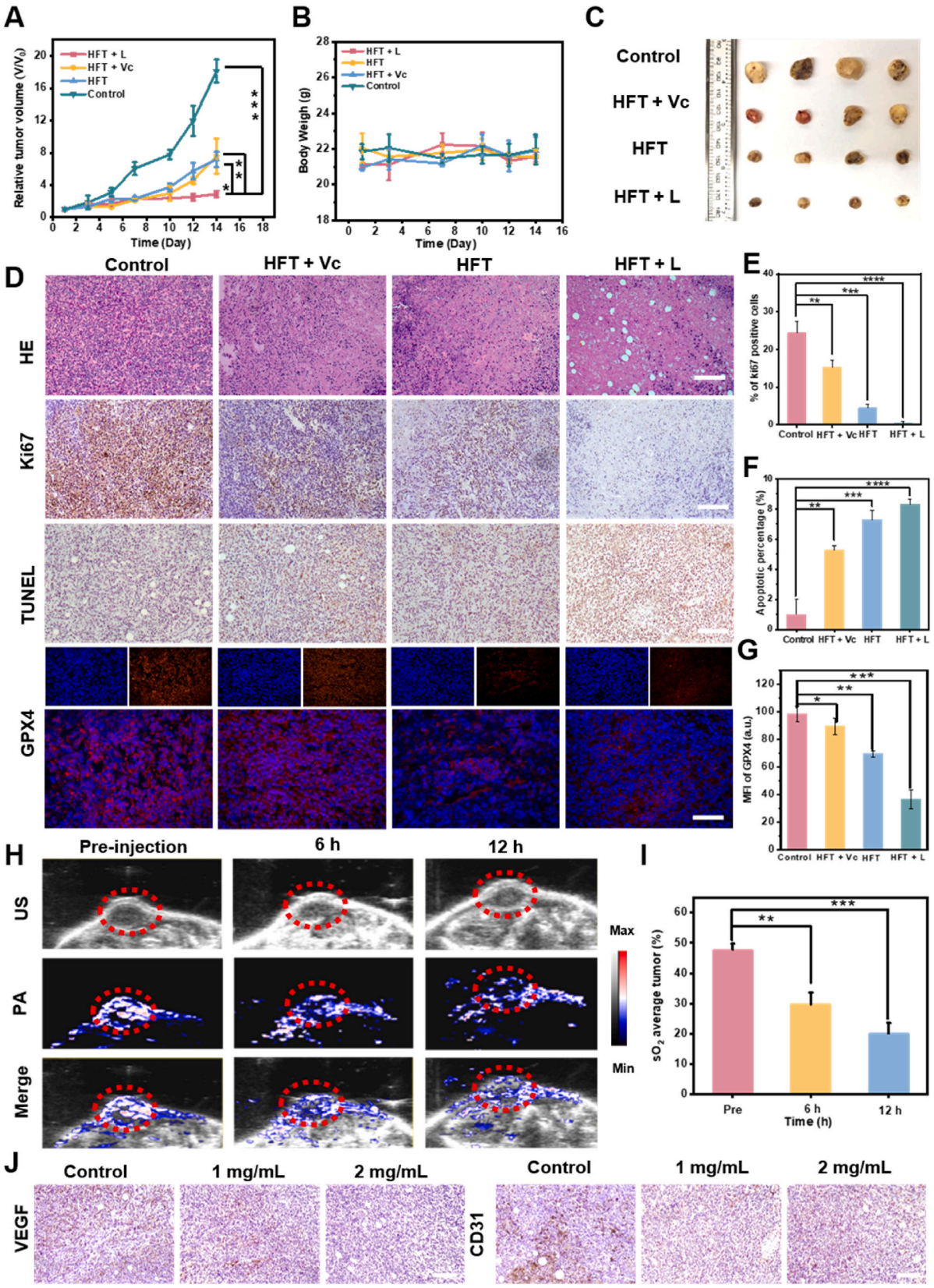

Fig. 6. In vivo cascade-amplified tumor therapy. (A) Relative tumor volume changes of all mice during treatments. (B) Body weight variation of all mice during treatments. (C) Photo of tumors collected at day 14. (D–G) H&E, Ki67, TUNEL and GPX4 staining of tumor slices from different treatment groups after 14 days therapy. (H) In vivo PA and US imaging of oxyhemoglobin saturation status (SO_2) in tumor tissue before and after 6 h and 12 h intratumoral injection of HFT. (I) Time-dependent sO_2 before and after HFT treatment for 6 h and 12 h. (J) VEGF and CD31 IHC staining of tumor sections after treatment with different concentrations of HFT. (Scale bar: 100 μm). Mean ± SD (n = 3). *p < 0.05, **p < 0.01, ***p < 0.001. Student's t-test.

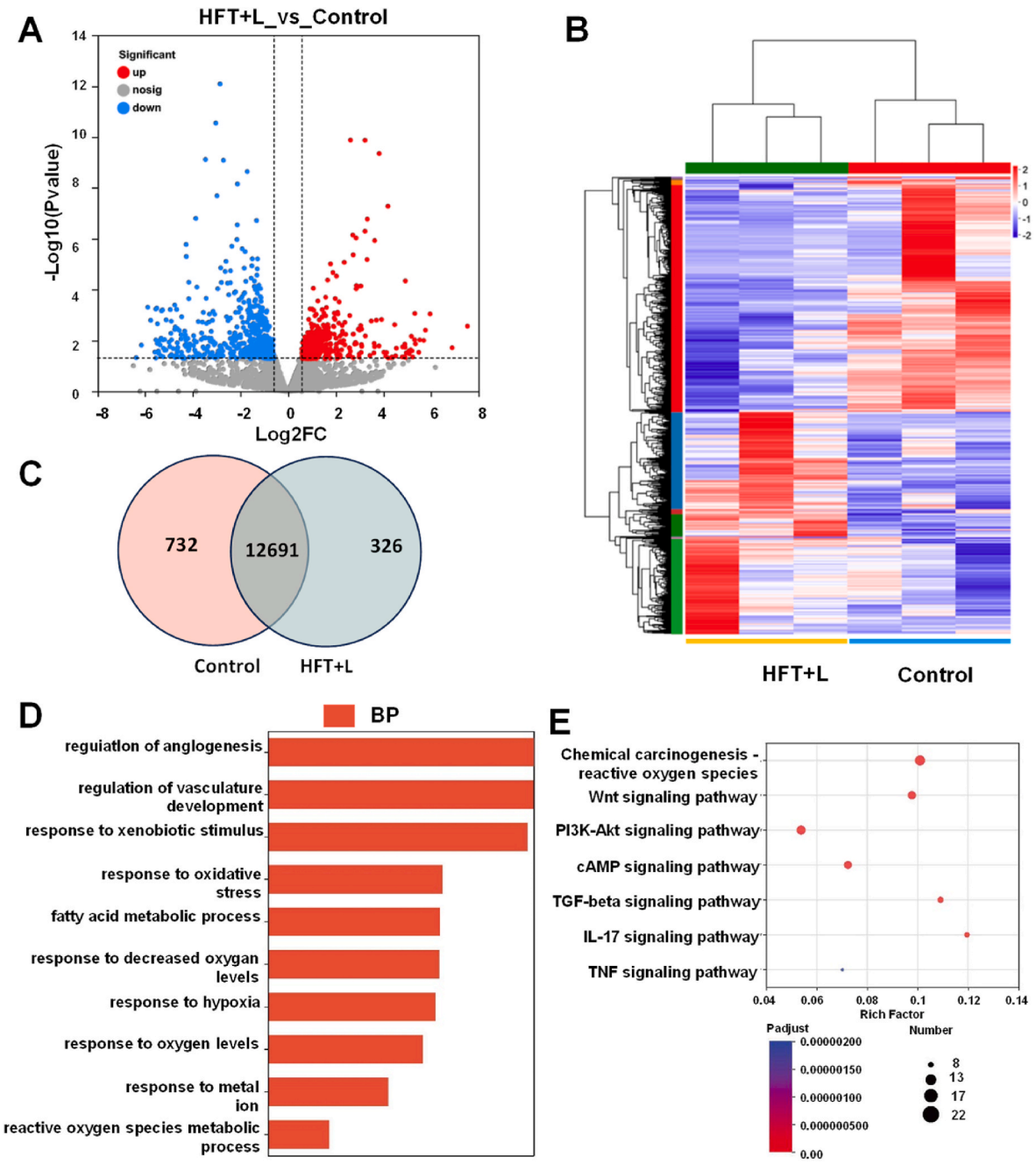

Fig. 7. RNA sequencing analysis. (A) Volcano plot of differentially regulated genes between the HFT + L and Control (PBS) group. (B) Heat map of expressed genes involved in the therapeutic progress. (C) Venn diagram of differentially expressed genes in HFT + L and PBS group. (D) GO enrichment analysis of biological processes for differentially expressed genes. (E) KEGG enrichment analysis for differentially expressed genes.

Fe-HMME nanoplatform, in combination with near-infrared (NIR) irradiation, can achieve highly efficient destruction of cancer cells and tumor inhibition.

4. Conclusion

In summary, we have developed a self-assembled drug-free nanoplatform that is activated by the tumor microenvironment (TME). These HFT exhibit a pH-driven butterfly effect in the TME, inducing ferroptosis and apoptosis of tumor tissue through cascade-amplified photodynamic therapy by ROS-mediated oxidative stress, GSH depletion, and GPX4 downregulation. The HFT nanoplatforms exhibit quenched MR and excellent photosensitization under neutral conditions, but recover MR imaging, chemotherapy and CDT functions in an acidic TME condition. This pH-driven "butterfly effect" reinforces the PDT and achieve cascade-amplified tumor therapy by MRI switch. This nanoplatform has excellent clinical PDT application prospects and benefits from the TME metabolism and endogenous component of degradation, compensating the tissue penetration restriction and poor treatment efficacy from PDT monotherapy.

CRediT authorship contribution statement

Botao Qu: Writing – review & editing, Writing – original draft, Funding acquisition, Conceptualization. **Qian Wang:** Writing – original draft, Validation, Methodology, Data curation. **Yuxin Zhou:** Writing – review & editing, Formal analysis, Conceptualization. **Xiaogang Ning:** Methodology, Data curation. **Qian Wang:** Investigation, Data curation.

Ziyi Zhou: Validation, Investigation. **Peirong Bai:** Visualization. **Ruiping Zhang:** Writing – review & editing, Supervision, Funding acquisition, Conceptualization.

Declaration of competing interest

The authors declare that they have no known competing financial interests or personal relationships that could have appeared to influence the work reported in this paper.

Acknowledgements

B.T.Q, and Q.W. contributed equally to this work. We acknowledge the Medical Experimental Center of Shanxi Bethune Hospital for providing the necessary equipment for this work. This work has been financially supported by the National Key R&D Program of China, 2023YFC3402800, National Natural Science Foundation of China (No: 82120108016, 82071987), Key Laboratory of Nano-imaging and Drug-loaded Preparation of Shanxi Province (NO: 202104010910010), and Natural Science Foundation of Shanxi Province (No. 202403021211183).

Appendix A. Supplementary data

Supplementary data to this article can be found online at https://doi.org/10.1016/j.mtbio.2025.101691.

Data availability

Data will be made available on request.

References

[1] A.B. Ormond, H.S. Freeman, Dye sensitizers for photodynamic therapy, Materials 6 (3) (2013) 817–840, https://doi.org/10.3390/ma6030817.
[2] D. Van Straten, V. Mashayekhi, H.S. De Bruijn, S. Oliveira, D.J. Robinson, Oncologic photodynamic therapy: basic principles, current clinical status and future directions, Cancers 9 (2) (2017) 19, https://doi.org/10.3390/cancers9020019.
[3] G.M. Cramer, K.A. Cengel, T.M. Busch, Forging forward in photodynamic therapy, Cancer Res. 82 (4) (2022) 534–536, https://doi.org/10.1158/0008-5472.CAN-21-4122.
[4] S.S. Lucky, K.C. Soo, Y. Zhang, Nanoparticles in photodynamic therapy, Chem. Rev. 115 (4) (2015) 1990–2042, https://doi.org/10.1021/cr5004198.
[5] T.C. Pham, V.-N. Nguyen, Y. Choi, S. Lee, J. Yoon, Recent strategies to develop innovative photosensitizers for enhanced photodynamic therapy, Chem. Rev. 121 (21) (2021) 13454–13619, https://doi.org/10.1021/acs.chemrev.1c00381.
[6] J. Karges, Clinical development of metal complexes as photosensitizers for photodynamic therapy of cancer, Angew. Chem., Int. Ed. 61 (5) (2022) e202112236, https://doi.org/10.1002/anie.202112236.
[7] B.C. Dickinson, C.J. Chang, Chemistry and biology of reactive oxygen species in signaling or stress responses, Nat. Chem. Biol. 7 (8) (2011) 504–511, https://doi.org/10.1038/nchembio.607.
[8] R.D. Almeida, B.J. Manadas, A.P. Carvalho, C.B. Duarte, Intracellular signaling mechanisms in photodynamic therapy, Biochimica et biophysica acta, Biochim. Biophys. Acta. 1704 (2) (2004) 59–86, https://doi.org/10.1016/j.bbcan.2004.05.003.
[9] Z. Zhou, J. Song, R. Tian, Z. Yang, G. Yu, L. Lin, G. Zhang, W. Fan, F. Zhang, G. Niu, L. Nie, X. Chen, Activatable singlet oxygen generation from lipid hydroperoxide nanoparticles for cancer therapy, Angew. Chem., Int. Ed. 56 (23) (2017) 6492–6496, https://doi.org/10.1002/anie.201701181.
[10] J. Xie, Y. Wang, W. Choi, P. Jangili, Y. Ge, Y. Xu, J. Kang, L. Liu, B. Zhang, Z. Xie, J. He, N. Xie, G. Nie, H. Zhang, J.S. Kim, Chem. Overcoming barriers in photodynamic therapy harnessing nano-formulation strategies, Soc. Rev. 50 (16) (2021) 9152–9201, https://doi.org/10.1039/d0cs01370f.
[11] G. Gunaydin, M.E. Gedik, S. Ayan, Photodynamic therapy-current limitations and novel approaches, Front. Chem. 9 (2021) 691697, https://doi.org/10.3389/fchem.2021.691697.
[12] S. Yu, C. Wang, J. Yu, J. Wang, Y. Lu, Y. Zhang, X. Zhang, Q. Hu, W. Sun, C. He, X. Chen, Z. Gu, Photodynamic therapy-current limitations and novel approaches, Front. Chem. 9 (2021) 691697, https://doi.org/10.3389/fchem.2021.691697.
[13] J. Zhu, Y. Zhang, Z. Li, X. Bao, Y. Zhou, B. Ma, Y. Xie, P. Yan, Z. Wu, Q. Zhang, J. J. Zou, X. Chen, Tumor-microenvironment-responsive poly-prodrug encapsulated semiconducting polymer nanosystem for phototherapy-boosted chemotherapy, Mater. Horiz. 10 (8) (2023) 3014–3023, https://doi.org/10.1039/d3mh00242j.
[14] Y. Zhang, Z. Dong, Y. Hao, Y. Gong, C. Wang, Y. Yan, M. Chen, Y. Wu, Q. Li, Z. Liu, L. Feng, Piezopotential-driven simulated electrocatalytic nanosystem of ultrasmall MoC quantum dots encapsulated in ultrathin N-doped graphene vesicles for superhigh H_2 production from pure water, Nano Energy 75 (2020) 104990, https://doi.org/10.1016/j.nanoen.2020.104990.
[15] J.E. Bader, K. Voss, J.C. Rathmell, Targeting metabolism to improve the tumor microenvironment for cancer immunotherapy, Mol. Cell 78 (6) (2020) 1019–1033, https://doi.org/10.1016/j.molcel.2020.05.034.
[16] M. Certo, C.-H. Tsai, V. Pucino, P.-C. Ho, C. Mauro, Lactate modulation of immune responses in inflammatory versus tumour microenvironments. Nature reviews, Nat. Rev. Immunol. 21 (3) (2021) 151–161, https://doi.org/10.1038/s41577-020-0406-2.
[17] C. Wang, Z. Dong, Y. Hao, Y. Zhu, J. Ni, Q. Li, B. Liu, Y. Han, Z. Yang, J. Wan, K. Yang, Z. Liu, L. Feng, Coordination polymer-coated CaCO3 reinforces radiotherapy by reprogramming the immunosuppressive metabolic microenvironment, Adv. Mater. 34 (3) (2022) 2106520, https://doi.org/10.1002/adma.202106520.
[18] J.-Y. Su, W.-H. Li, Y.-M. Li, Chem. New opportunities for immunomodulation of the tumour microenvironment using chemical tools, Chem. Soc. Rev. 51 (18) (2022) 7944–7970, https://doi.org/10.1039/d2cs00486k.
[19] C. Wang, S. Ding, S. Wang, Z. Shi, N.K. Pandey, L. Chudal, L. Wang, Z. Zhang, Y. Wen, H. Yao, L. Lin, W. Chen, L. Xiong, Endogenous tumor microenvironment-responsive multifunctional nanoplatforms for precision cancer theranostics, Coord. Chem. Rev. 426 (2021) 213529, https://doi.org/10.1016/j.ccr.2020.213529.
[20] F. Gong, N. Yang, X. Wang, Q. Zhao, Q. Chen, Z. Liu, L. Cheng, Tumor microenvironment-responsive intelligent nanoplatforms for cancer theranostics, Nano Today 32 (2020) 100851, https://doi.org/10.1016/j.nantod.2020.100851.
[21] S. Sun, Q. Chen, Z. Tang, C. Liu, Z. Li, A. Wu, H. Lin, Tumor microenvironment stimuli-responsive fluorescence imaging and synergistic cancer therapy by carbon-dot-Cu(2+) nanoassemblies, Angew. Chem., Int. Ed. 59 (47) (2020) 21041–21048, https://doi.org/10.1002/anie.202007786.
[22] Y. Li, Y. Wu, J. Chen, J. Wan, C. Xiao, J. Guan, X. Song, S. Li, M. Zhang, H. Cui, T. Li, X. Yang, Z. Li, X. Yang, A simple glutathione-responsive turn-on theranostic nanoparticle for dual-modal imaging and chemo-photothermal combination therapy, Nano Lett. 19 (8) (2019) 5806–5817, https://doi.org/10.1021/acs.nanolett.9b02769.
[23] W. Zhen, Y. Liu, W. Wang, M. Zhang, W. Hu, X. Jia, C. Wang, X. Jiang, Specific "Unlocking"of a nanozyme-based butterfly effect to break the evolutionary fitness of chaotic tumors, Angew. Chem., Int. Ed. 59 (24) (2020) 9491–9497, https://doi.org/10.1002/anie.201916142.
[24] Y. Shao, Z. Wang, Y. Hao, X. Zhang, N. Wang, K. Chen, J. Chang, Q. Feng, Z. Zhang, Cascade catalytic nanoplatform based on "butterfly effect" for enhanced immunotherapy, Adv. Healthcare Mater. 10 (8) (2021) 2002171, https://doi.org/10.1002/adhm.202002171.
[25] Z. Hao, X. Cheng, C. Cong, X. Zhang, W. Zhang, Q. Zhao, S. Wang, D. Gao, Nanoreactor of"butterfly effect" inciting a triple interlocked combination of starvation/chemo/metal ion therapy by remodeling tumor microenvironment, Chem. Eng. J. 405 (2021) 126571, https://doi.org/10.1016/j.cej.2020.126571.
[26] M.P. Melancon, M. Zhou, C. Li, Cancer theranostics with near-infrared light-activatable multimodal nanoparticles, Acc. Chem. Res. 44 (10) (2011) 947–956, https://doi.org/10.1021/ar200022e.
[27] Q. Zhang, M. He, X. Zhang, H. Yu, J. Liu, Y. Guo, J. Zhang, X. Ren, H. Wang, Y. Zhao, Tumor microenvironment activated chemodynamic–photodynamic therapy by multistage self - assembly engineered protein nanomedicine, Adv. Funct. Mater. 32 (17) (2022) 2112251, https://doi.org/10.1002/adfm.202112251.
[28] Y. Yang, Y. Liu, D. Tu, M. Chen, Y. Zhang, H. Gao, X. Chen, Tumor-microenvironment-responsive biodegradable nanoagents based on lanthanide nucleotide self-assemblies toward precise cancer therapy, Angew. Chem., Int. Ed. 61 (14) (2022) 202116983, https://doi.org/10.1002/anie.202116983.
[29] J. Xu, J. Wang, J. Ye, J. Jiao, Z. Liu, C. Zhao, B. Li, Y. Fu, Metal-coordinated supramolecular self-assemblies for cancer theranostics, Adv. Sci. 8 (16) (2021) 2101101, https://doi.org/10.1002/advs.202101101.
[30] Z. Ren, S. Sun, R. Sun, G. Cui, L. Hong, B. Rao, A. Li, Z. Yu, Q. Kan, Z. Mao, A metal-polyphenol-coordinated nanomedicine for synergistic cascade cancer chemotherapy and chemodynamic therapy, Adv. Mater. 32 (6) (2020) 1906024, https://doi.org/10.1002/adma.201906024.
[31] Y. Li, Q. Zou, C. Yuan, S. Li, R. Xing, X. Yan, Amino acid coordination driven self-assembly for enhancing both the biological stability and tumor accumulation of curcumin, Angew. Chem., Int. Ed. 57 (52) (2018) 17084–17088, https://doi.org/10.1002/anie.201810087.
[32] H. Zhang, K. Liu, S. Li, X. Xin, S. Yuan, G. Ma, X. Yan, Self-assembled minimalist multifunctional theranostic nanoplatform for magnetic resonance imaging-guided tumor photodynamic therapy, ACS Nano 12 (8) (2018) 8266–8276, https://doi.org/10.1021/acsnano.8b03529.
[33] P. Zhang, J. Wang, H. Chen, L. Zhao, B. Chen, C. Chu, H. Liu, Z. Qin, J. Liu, Y. Tan, X. Chen, G. Liu, Tumor microenvironment-responsive ultrasmall nanodrug generators with enhanced tumor delivery and penetration, J. Am. Chem. Soc. 140 (44) (2018) 14980–14989, https://doi.org/10.1021/jacs.8b09396.
[34] S. Dutt, I. Hamza, T.B. Bartnikas, Molecular mechanisms of iron and heme metabolism, Annu. Rev. Nutr. 42 (2022) 311–335, https://doi.org/10.1146/annurev-nutr-062320-112625.
[35] X. Shan, S. Li, B. Sun, Q. Chen, J. Sun, Z. He, C. Luo, Ferroptosis-driven nanotherapeutics for cancer treatment, J. Contr. Release 319 (2020) 322–332, https://doi.org/10.1016/j.jconrel.2020.01.008.
[36] P. Sun, F. Qu, C. Zhang, P. Cheng, X. Li, Q. Shen, D. Li, Q. Fan, NIR-II excitation phototheranostic platform for synergistic photothermal therapy/chemotherapy/

chemodynamic therapy of breast cancer bone metastases, Adv. Sci. 9 (33) (2022) 2204718, https://doi.org/10.1002/advs.202204718.
[37] D. Gupta, S.P. Treon, Y. Shima, T. Hideshima, K. Podar, Y.T. Tai, B. Lin, S. Lentzsch, F.E. Davies, D. Chauhan, R.L. Schlossman, P. Richardson, P. Ralph, L. Wu, F. Payvandi, G. Muller, D.I. Stirling, K.C. Anderson, Adherence of multiple myeloma cells to bone marrow stromal cells upregulates vascular endothelial growth factor secretion: therapeutic applications, Leukemia 15 (12) (2001) 1950–1961, https://doi.org/10.1038/sj.leu.2402295.
[38] H. Zheng, L. Xing, Y. Cao, S. Che, Coordination bonding based pH-responsive drug delivery systems, Coord. Chem. Rev. 257 (2013) 1933–1944, https://doi.org/10.1016/j.ccr.2013.03.007.
[39] M. Li, W. Sun, R. Tian, J. Cao, Y. Tian, B. Gurram, J. Fan, X. Peng, Smart J-aggregate of cyanine photosensitizer with the ability to target tumor and enhance photodynamic therapy efficacy, Biomaterials 269 (2021) 120532, https://doi.org/10.1016/j.biomaterials.2020.120532.
[40] Y. Li, T. Ma, H. Jiang, W. Li, D. Tian, J. Zhu, Z. Li, Anionic cyanine J-type aggregate nanoparticles with enhanced photosensitization for mitochondria-targeting tumor phototherapy, Angew. Chem. Int. Ed. 61 (24) (2022) 202203093, https://doi.org/10.1002/anie.202203093.
[41] H. Li, H. Zhu, C.-j. Xu, J. Yuan, Cleavage of BID by caspase 8 mediates the mitochondrial damage in the fas pathway of apoptosis, Cell 94 (4) (1998) 491–501, https://doi.org/10.1016/S0092-8674(00)81590-1.
[42] X. Meng, D. Li, L. Chen, H. He, Q. Wang, C. Hong, J. He, X. Gao, Y. Yang, B. Jiang, G. Nie, X. Yan, L. Gao, K. Fan, High-performance self-cascade pyrite nanozymes for apoptosis-ferroptosis synergistic tumor therapy, ACS Nano 15 (3) (2021) 5735–5751, https://doi.org/10.1021/acsnano.1c01248.
[43] Y. Zheng, X. Li, C. Dong, L. Ding, H. Huang, T. Zhang, Y. Chen, R. Wu, Ultrasound-augmented nanocatalytic ferroptosis reverses chemotherapeutic resistance and induces synergistic tumor nanotherapy, Adv. Funct. Mater. 32 (4) (2022) 2107529, https://doi.org/10.1002/adfm.202107529.
[44] Y. Li, W. Fan, X. Gu, S. Liu, T. He, S. Gou, W. Meng, M. Li, X. Liu, Y. Ren, C. Qi, K. Cai, Biodegradable ferric phosphate nanocarriers with tumor-specific activation and glutathione depletion for tumor self-enhanced ferroptosis and chemotherapy, Adv. Funct. Mater. 34 (21) (2024) 231540, https://doi.org/10.1002/adfm.202313540.
[45] W. Liu, R. Shao, L. Guo, J. Man, C. Zhang, L. Li, H. Wang, B. Wang, L. Guo, S. Ma, B. Zhang, H. Diao, Y. Qin, L. Yan, Precise design of TiO2@CoOx heterostructure via atomic layer deposition for synergistic sono-chemodynamic oncotherapy, Adv. Sci. 11 (14) (2024) 2304046, https://doi.org/10.1002/advs.202304046.
[46] L. Zhao, F. Chang, Y. Tong, J. Yin, J. Xu, H. Li, L. Du, Y. Jiang, A multifunctional bimetallic nanoplatform for synergic local hyperthermia and chemotherapy targeting HER2-positive breast cancer, Adv. Sci. 11 (16) (2024) 2308316, https://doi.org/10.1002/advs.202308316.
[47] Q. Cheng, X. Shi, Y. Chen, Q. Li, J. Wang, H. Li, L. Wang, Z. Wang, Tumor microenvironment-activatable nanosystem capable of overcoming multiple therapeutic obstacles for augmenting immuno/metal-ion therapy, ACS Nano 18 (12) (2024) 8996–9010, https://doi.org/10.1021/acsnano.3c12745.
[48] C. Zhang, J. Huang, Z. Zeng, S. He, P. Cheng, J. Li, K. Pu, Catalytical nano-immunocomplexes for remote-controlled sono-metabolic checkpoint trimodal cancer therapy, Nat. Commun. 13 (1) (2022) 3468, https://doi.org/10.1038/s41467-022-31044-6.